IEEE Sensors Council

Hyperspectral Imaging based Corrosion Detection in Nuclear Packages

Jaime Zabalza, Paul Murray, Stuart Bennett, Andrew Campbell, Stephen Marshall, Jinchang Ren, Yijun Yan, Robert Bernard, Steve Hepworth, Simon Malone, Neil Cockbain, Douglas Offin, and Craig Holliday

***Abstract*—In the Sellafield nuclear site, intermediate level waste and special nuclear material is stored above ground in stainless steel packages or containers, with thousands expected to be stored for several decades before permanent disposal in a geological disposal facility. During this intermediate storage, the packages are susceptible to corrosion, which can potentially undermine their structural integrity. Therefore, long term monitoring is required. In this work, hyperspectral imaging (HSI) was evaluated as a non-destructive tool for detecting corrosion on stainless steel surfaces. Real samples from Sellafield, including stainless steel 1.4404 (known as 316L) and 2205 plates from the Sellafield atmospheric testing corrosion site, were imaged in the experiments, measuring the spectral responses for corrosion in the visible near-infrared (VNIR, 400-1000 nm) and short-wave-infrared (SWIR, 900-2500 nm) regions. Based on the spectral responses observed, a new concept denoted as Corrosion Index (CI) was introduced and evaluated to estimate corrosion maps. With the CI, every pixel in the hyperspectral image is given a value between zero and one, aimed at representing corrosion intensity for a given location of the sample. Results suggest that HSI, combined with our proposed CI analysis techniques, could be used for effective automated detection of corrosion in nuclear packages.**

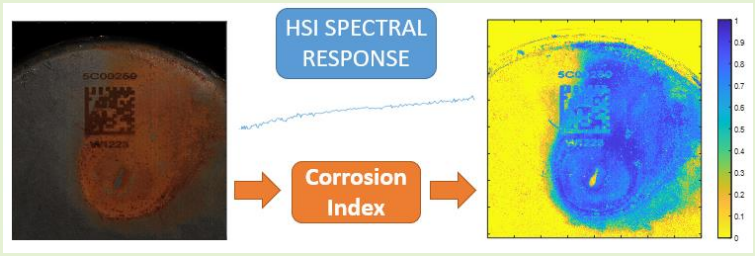

***Index Terms*—Corrosion, hyperspectral imaging, nuclear packages, stainless steel**

I. Introduction

THE Sellafield nuclear site (Cumbria, UK) has a number of package configurations (cans, drums, and boxes) for storing intermediate level waste and special nuclear material. These packages, usually high-quality stainless steel containers, are filled with nuclear material and nuclear waste, and placed in protected stores above ground at Sellafield for intermediate storage before a geological disposal facility is available for permanent disposal. It is anticipated that more than 150,000 packages will be stored for the next several decades.

During this period, the packages have to be monitored to ensure that their performance is as expected. While the stainless steel used in the manufacturing of storage packages shows good resistance, these containers are still susceptible to different sources of corrosion leading to pitting, precursor of the atmospherically induced stress corrosion cracking, or even corrosion related to Polyvinyl Chloride (PVC) degradation, when corrosive hydrochloric acid is generated from the PVC plasticized films used in some containers [1-2].

Corrosion can have a significant impact on the structural integrity of the containers and, therefore, appropriate monitoring is required. However, suspect packages at Sellafield are currently inspected manually, which is challenging, subjective and time consuming. This could be potentially improved by introducing automated inspections based on different technologies. The state of the art includes non-destructive methods based on Eddy current [3-6], microwave [7-9], corrosion sensors for undersea monitoring [10] or laser profiling techniques [11] for detecting corrosion-related defects. Imaging technologies are of particular interest, as they can easily capture data across large surface areas. In recent years, diverse image processing approaches have been proposed for the non-destructive detection of corrosion in several diverse applications. These approaches include conventional imaging (RGB) and, more recently, hyperspectral imaging (HSI), which has been claimed to have better potential for detecting corrosion [12], covering spectral information in the visible near-infrared (VNIR) and short-wave-infrared (SWIR) regions of the electromagnetic spectrum.

This research was funded by Sellafield Ltd and the National Nuclear Laboratory through the Game Changers Innovation Programme co-delivered by FIS360 Ltd (project GC-142).

J. Zabalza, P. Murray, S. Bennett, A. Campbell, and S. Marshall are with Department of Electronic and Electrical Engineering, University of Strathclyde, Glasgow, G1 1XW, UK (e-mail: j.zabalza@strath.ac.uk).

J. Ren and Y. Yan are with National Subsea Centre, Robert Gordon University, Aberdeen, AB21 0BH, UK.

R. Bernard, S. Hepworth, and S. Malone are with Sellafield Ltd, Sellafield, Cumbria, CA20 1PG, UK.

N. Cockbain, D. Offin, and C. Holliday are with National Nuclear Laboratory Ltd, Workington, CA14 3TQ, UK.

The main advantage of HSI is its capability to capture both spectral and spatial data simultaneously. While RGB spectral resolution is limited to three channels (red, green, and blue), covering only color, HSI provides hundreds of channels covering not only the visible range but also the near infrared. However, HSI has been barely explored, and the current state of the art has focused on samples prepared in the lab (lab-induced corrosion). Therefore, this corrosion may not be representative of the real corrosion developed onsite for years and even decades. In this work, HSI was evaluated for corrosion detection using real samples from the Sellafield site. This included plates from the Sellafield atmospheric testing corrosion site, which was installed in 1991 to simulate the worst-case environments within the stores.

The aim of the work described in this paper is two-fold, contributing to the state of the art by:

- Reporting spectral responses of real/onsite stainless steel samples both in the VNIR and SWIR regions (400-2500 nm), with Headwall VNIR E-series [13] and SWIR-640 [14] sensors.

- Introducing the Corrosion Index (CI) concept to estimate corrosion. This estimation is currently data-driven, being based on the observed hyperspectral responses. However, the underlying chemical characterization will be investigated in the future for incorporating chemical-based prior knowledge.

The rest of this manuscript is organized as follows: Section 2 summarizes the related work developed for the detection of corrosion using both conventional imaging and HSI. Section 3 describes the different samples used in the experiments, along with the hyperspectral systems for data acquisition. Then, Section 4 presents the different experiments undertaken with related analysis and results. Finally, some conclusions are drawn in Section 5.

II. Related Work

A. Conventional Imaging

The evaluation of conventional imaging for the detection of corrosion is a relatively recent research topic, which has targeted different materials and applications. For example, an initial work was published in 2009, where Chen et al. investigated the detection of rust in bridges using conventional images in 14 different color spaces. This included red-green-blue (RGB), L*a*b*, and many others [15], where L*a*b* achieved the best performance filtering out light effects. Some years later, in 2014, Bonnín-Pascual et al. acknowledged the reduced amount of contributions in this topic, introducing texture (roughness) analysis in RGB images based on the Grey Level Co-occurrence Matrix [16] for corrosion detection.

Since then, there has been a number of publications in which different color spaces and algorithms for corrosion detection or classification have been investigated, including the hue-saturation-intensity (H-S-I) color space with Support Vector Machines (SVMs) [17], and the hue-saturation-value (H-S-V) color space with deep learning [18]. In 2015, Feliciano et al. evaluated six textural characteristics in RGB images [19], while in 2017, Ahuja et al. [20] developed an interesting survey on corrosion on metallic surfaces considering color, texture, noise, clustering, segmentation, enhancement, and wavelet transformation features.

More recently, research has focused on optimizing the image processing pipeline, where different combinations of refined color and texture features along with diverse classifiers have been evaluated, including 2D Gabor filters and Principal Component Analysis (PCA) [21], morphology [22], Xu segmentation [23], Multi-Layer Perceptron [24], and some others [25-29], where recent deep-learning-based methods [30-32] could be further explored to this purpose.

However, most of this work is highly limited to the reduced broadband spectra of the information in conventional imaging (RGB), and the potential of HSI [33], a promising technology in this field, still needs to be explored.

B. Hyperspectral Imaging (HSI)

Research using HSI for corrosion detection on metals is very limited and significant work can only be found in the last 6 years. In 2016, Simova et al. reported the spectral response of microbially induced corrosion in the VNIR region [34]. In 2018, Rowley published a PhD thesis reporting responses of corrosion products in the VNIR, also including Raman spectroscopy, where it was suggested that HSI has better potential for detecting corrosion than conventional imaging at the cost of higher complexity [12]. In the same year, Catelli et al. [35] investigated the use of HSI SWIR for corrosion detection in bronze sculptures.

In 2019, Antony et el. [36] published a work for inspection of corrosion in difficult-to-access areas by a probe-based hyperspectral imager, work which was extended in [37]. In 2020, Kobayashi et al. [38] stated that different corrosion products including Goethite, Akageneite, Lepidocrocite, and iron oxide can be recognized in the VNIR region, and Chen's work [39] used SVM to classify samples with lab-induced corrosion (three categories), reporting spectral responses not only in the VNIR but also in the SWIR region

In 2021, Lavadiya et al. [40] evaluated corrosion in ASTM A572 structural steel with lab-prepared samples, using PCA and SVM to classify VNIR spectra into either acid corrosion (HCl), salt corrosion (NaCl), sulphate corrosion (Na_2SO_4), painted coating, or no-corrosion. In the same year, Yang et al. used k-Nearest Neighbor and Partial Least Square Discriminant Analysis to recognize different intensities of corrosion in steel transmission towers via lab-induced corrosion samples at 4 time categories (48h, 96h, 192h, and 384h) [41]. Finally, in 2022, De Kerf et al. investigated the NIR region (up to 1700 nm) to identify four corrosion products including Goethite, Magnetite, Lepidocrocite, and Hematite in lab-prepared samples [42].

The previously described work represents the current state of the art in using the hyperspectral technology for corrosion detection. Therefore, plenty of research is still required to understand how this technology can be effectively used for this purpose. While some spectral responses of corrosion have already been reported [12], [34], [40], further investigation is needed to support and confirm these findings in both VNIR and SWIR regions. Additionally, the samples evaluated in the literature present lab-induced corrosion [39], [40], [41], [42], which may differ from the corrosion developed onsite over the years. In this work, five different partially corroded stainless steel samples, two of them corroded onsite at Sellafield, are evaluated to report spectral responses of corrosion at different stages in its lifecycle.

III. Materials and Methods

A. Samples

Hyperspectral images were captured for a total of five stainless steel samples, from which spectral responses were evaluated. These samples, provided by Sellafield, were selected because they have different backgrounds and histories, allowing the evaluation of corrosion from different perspectives. However, no ground truth (e.g., chemical characterization via laser-induced breakdown spectroscopy) was available by the time this work was conducted. These samples are described as follows.

The 316L distressed sample ('316Ld') is an austenitic stainless steel plate (35 x 20 cm), which has been exposed for 4 years in the atmospheric corrosion site at Sellafield. This sample was originally distressed across 4 areas that still remain clearly visible (see Fig. 1(a) and 1(b)). A visual inspection reveals the presence of some specific areas with clear visible corrosion, as well as a no-corrosion background.

Two stainless steel grade 2205 duplex samples were also used in the experiments (Fig. 1(c) and 1(d)). One is a control sample ('control 2205', 20 x 20 cm) which has been stored indoors at Sellafield for 29 years. The other is an exposed sample ('exposed 2205', 20 x 20 cm), expected to show some corrosion after a 29-year exposure at the Sellafield atmospheric testing corrosion site. The exposed sample shows several corrosion spots across its surface.

Another sample of interest is the '316L filter' (Fig. 1(f), 2 x 2 cm). This sample was extracted from a larger (and unused) 316L filter sheet provided by Sellafield. This filter configuration is normally present in the top side of many (breathable) containers. Unlike the rest of the samples evaluated in this work, the 316L filter presents lab-induced corrosion (a salt-bath at the University of Strathclyde was applied to achieve corrosion), and it was included in the analysis for comparison with the corrosion observed in real/onsite samples. Several corrosion and no-corrosion areas across the surface of this sample can be clearly identified.

Finally, the 'overpack' sample (Fig. 1(h), 32 cm height, 16 cm diameter) is a 316L stainless steel overpack can in which the base presents advanced corrosion. This corrosion is due to the exposure to PVC under lab conditions. A visual inspection reveals potentially different stages of corrosion across the base of the can, hence the interest in imaging the base of this particular sample. The other surfaces of the can were not imaged as no significant corrosion was found.

B. Hyperspectral Imaging Systems

Two different systems from Headwall Photonics Inc. [43] were used to capture the hyperspectral images of the samples under analysis. The overall spectral range covered by both systems included the VNIR and SWIR regions (400-2500 nm in total).

The Headwall VNIR-E series [13] (sCMOS detector) was used to gather data in the VNIR region (400-1000 nm) in 373 different spectral channels with a spectral resolution of ~1.63 nm, and 1600 spatial pixels.

Another Headwall system, the SWIR-640 [14] (MCT detector), captured data in the SWIR region (900-2500 nm) in 272 spectral channels or bands with a spectral resolution of ~6 nm, and 640 spatial pixels. The ADC bit depth for both systems is 16 bits.

Both sensors required the same setup for data capturing (see Fig. 2), which involved a number of other elements too. Data

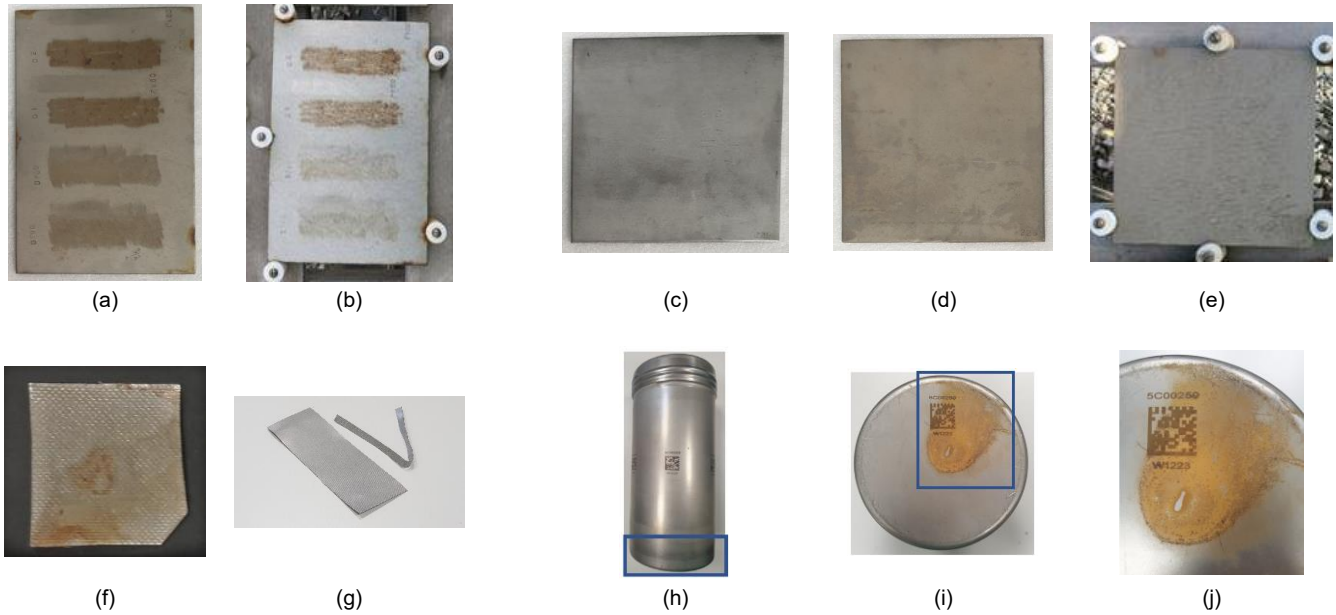

Fig. 1. Samples used during experiments.

Top left: Sample '316Ld' (35 x 20 cm) from the atmospheric testing corrosion site at Sellafield - (a) an image of the sample captured during the experiments, and (b) an image of the sample during exposure in the atmospheric testing corrosion site shown for reference (credit: Sellafield Ltd).

Top right: Samples 'control 2205' (20 x 20 cm) and 'exposed 2205' (20 x 20 cm) from the atmospheric testing corrosion site at Sellafield - (c) an image of the 'control 2205' sample, and (d) an image of the 'exposed 2205' sample, both captured during the experiments, and (e) an image of an exposed 2205 sample (different to the analyzed one) in the atmospheric testing corrosion site shown just for reference (credit: Sellafield Ltd).

Bottom left: Sample '316L filter' (2 x 2 cm) with corrosion induced at the University of Strathclyde - (f) an image of the sample captured during the experiments, and (g) an image of the larger sheet provided by Sellafield from which the sample was extracted.

Bottom right: Sample 'overpack' (32 cm height, 16 cm diameter) - (h) an image of the entire can, (i) an image of the base of the can, which is partially corroded, and (j) a zoomed-in image of the corroded area to be imaged.

acquisition was based on the push-broom technology [44], [45], which means that the sensors performed line scan at constant speed to capture the hyperspectral images. This line scan required relative movement between the sensor and the sample under study, which was achieved by placing the sample on the Headwall linear translation stage. Additionally, an adjustable broadband light source was needed to illuminate the sample and calibrate the sensors. Finally, a PC with Headwall software was used to control the system.

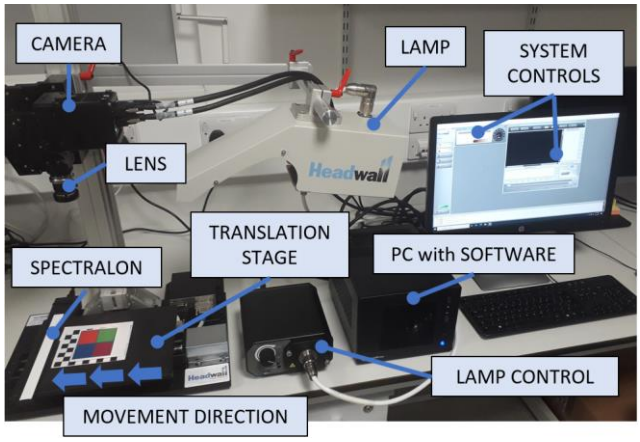

Fig. 2. Setup of the Headwall hyperspectral sensors for data capturing, which mainly includes sensor, translation stage, adjustable light source, and PC with common peripherals (screen, keyboard and mouse).

Data was captured after a standard calibration procedure using dark and white reference images [44]. The white reference was obtained using a Spectralon tile (bottom left corner in Fig. 2), and the dark reference by covering the lens. After calibration, hyperspectral images showed reflectance intensity normalized in the range [0-1] (zero for black or 0% reflectance, and one for white or 100% reflectance). The stand-off distance between the lens and samples was approximately 50 cm, which translates into spatial resolutions in the hyperspectral images of ~0.1 mm/pixel and ~0.3 mm/pixel for VNIR and SWIR, respectively (different resolutions due to the different specifications of the systems). Experiments with the overpack sample were an exception due to the height of the can, resulting in a stand-off distance of 18 cm, with spatial resolutions of ~0.05 mm/pixel and ~0.1 mm/pixel, respectively.

C. Corrosion Index Method

The evolution of corrosion over time could be modeled based on the evolutionary shape of the spectral responses, as it will be shown in Section IV.C. An accurate modeling would ideally require further analysis based on the underlying chemical characterization of the different corrosion products. While this ground truth information was not available for the evaluated samples, an initial modeling based on the evolution of the spectral responses is still possible. This modeling looks for an automated detection and estimation of corrosion purely based on hyperspectral data.

In order to detect and estimate corrosion through hyperspectral data, a new concept denoted as Corrosion Index (CI) is introduced in this work. The CI metric aims at representing the corrosion stage for a given pixel (a spectral response) in the image of a sample. The CI is a real value ($CI \in R^1, CI \in [0,1]$) between zero and one, where a value of zero or small values close to zero would represent a situation of no-corrosion, while a value of one or large values close to one would represent high/advanced corrosion. Therefore, the intermediate part of the CI scale would become the range of main interest, in which pre-corrosion or early corrosion, difficult to identify by the human eye, could be detected.

The CI is computed pixel-wise based on the spectral content and requires prior knowledge about the spectral response for advanced corrosion for a particular material (reference response ref), and two calibration coefficients a, b. The core algorithm of the CI compares the spectral response under analysis to the reference one (ref), and quantifies the difference between both. The CI can use different core algorithms to quantify this spectral difference, and it is expected that the algorithm will be different depending on the spectral range covered (VNIR, SWIR) and the type of material evaluated. In this work, the Angular Cosine Distance (ACD) [46] [47], defined as $ACD(input, ref) = 2cos^{-1}\left(\frac{input \cdot ref}{\|input\|\|ref\|}\right)/\pi$ was used for this (see Fig. 3).

The ACD measures the dissimilarity between an input spectral response and the reference response (ref), leading to a score $\in [0,1]$ in which smaller values indicate a high similarity of the responses. Therefore, the CI can be defined as:

$$CI = \begin{cases} \frac{(a - ACD(input,ref))}{(a-b)} & if\ ACD\_score \leq a \\ 0 & if\ ACD\_score > a \end{cases} \quad (1)$$

where a, b in Eq. 1 are two coefficients for the calibration of the CI. These coefficients implement a remapping of the ACD values, translating them to the CI scale ($CI \in [0,1]$). The remapping values play a key role and must be adjusted properly based on prior knowledge. The a and b coefficients represent the ideal ACD values corresponding to no-corrosion and advanced corrosion, respectively, for a particular material so that the relative ACD values can be translated into the absolute CI scale. In this work, the values of a and b were empirically adjusted based on the analysis of the samples under evaluation as both advanced corrosion and no-corrosion responses were available, allowing the estimation of these coefficients. In practical terms, as long as both advanced corrosion and no-corrosion responses are available and reliable for a given material, this empirical adjustment of a and b is enough for calibrating the CI, which can then be used for new samples and images of the same material.

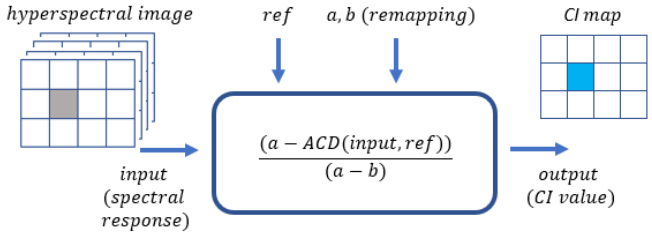

Fig. 3. Schematic representation of the CI modeling, with input, output, and prior knowledge.

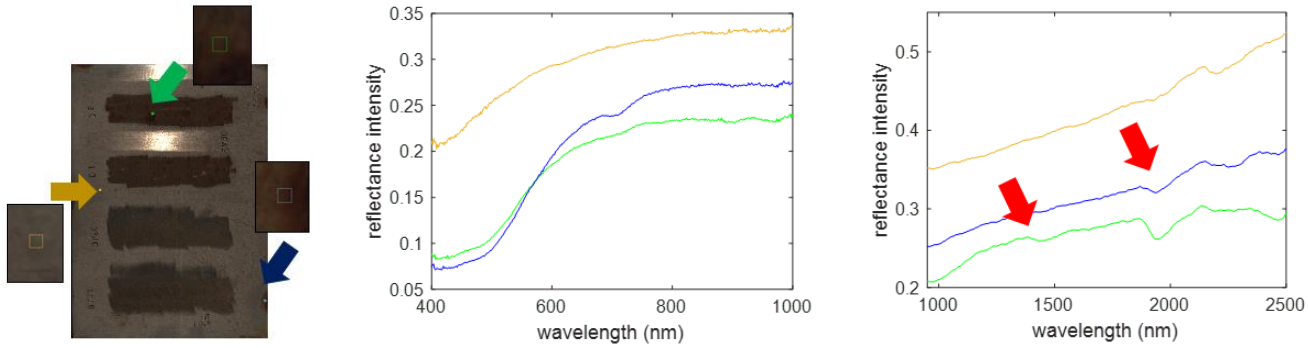

(a) (b) (c)

Fig. 4. Spectral responses from the 316Ld sample - (a) HSI composite image of the sample, highlighting the evaluated 10x10-pixel areas from which the responses are averaged, (b) spectral responses in the VNIR region, and (c) spectral responses in the SWIR region.

IV. Experiments and Results

A. Spectral Response of Corrosion on 316L

In this experiment, spectral responses from the 316Ld sample are reported. Fig. 4(b) shows three different spectral responses in the VNIR region. The first response (yellow color) was extracted from an apparent no-corrosion area in the background, and the other two spectral responses (green and blue) were extracted from clearly visible corroded areas. A direct comparison between these suggests that corrosion leads to spectral responses with a significant curve in the 400-700 nm range when compared to a much flatter response for the no-corrosion case. This finding correlates in some degree with previous work [12], [34], [40].

Fig. 4(c) shows SWIR spectral responses from the 316Ld sample at the same locations. Therefore, the response in yellow color comes from an area where no corrosion was observed, while the other two spectral responses (in green and blue colors) represent corroded areas. On this occasion, although there are differences in the responses (see red arrows in Fig. 4(c)), and some peaks could be linked to the presence of hydroxides [35] [39], key differential features are not conclusive without further analysis.

B. Spectral Response of Corrosion on 2205 Duplex

Spectral responses of the 2205 samples are also reported. Fig. 5(b) shows VNIR responses from different areas in the control 2205 sample. The three responses look relatively similar to each other except for a change in reflectance intensity, especially for the response shown in blue color, which is extracted from a

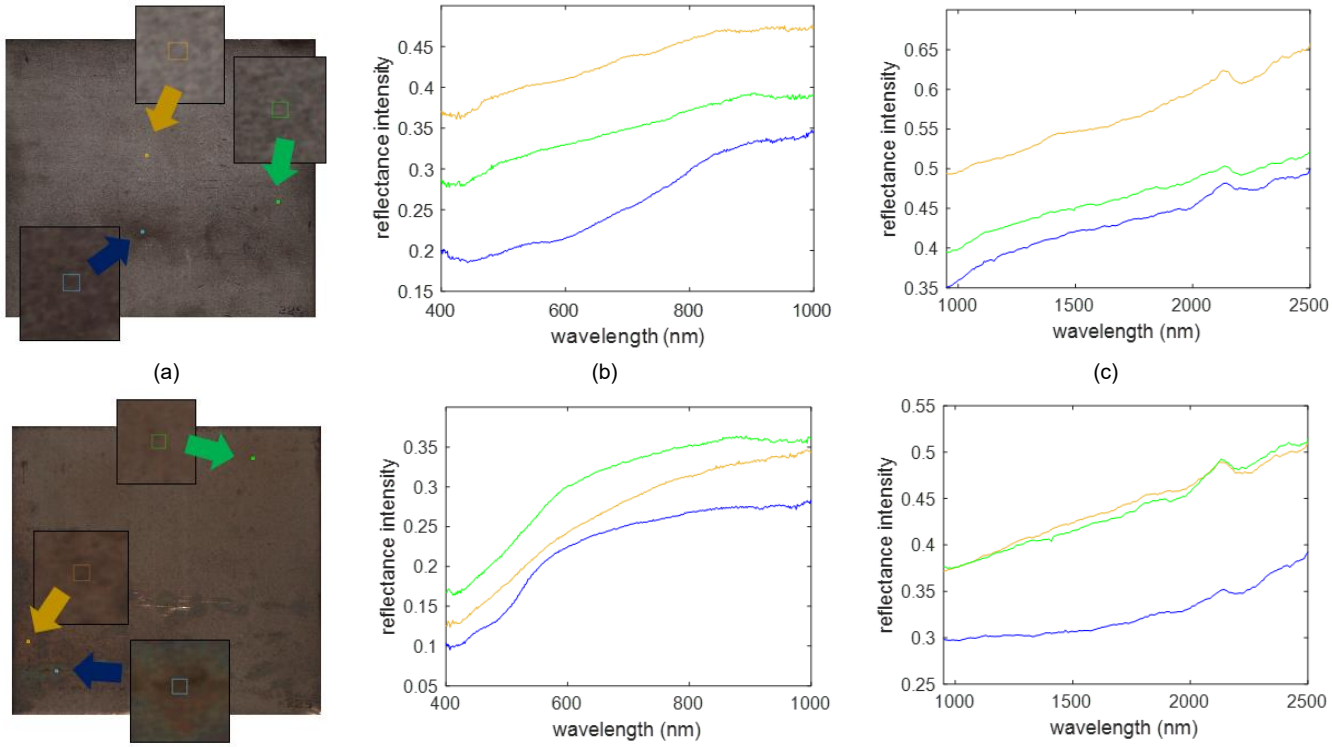

(a) (b) (c)

(d) (e) (f)

Fig. 5. Spectral responses from the control 2205 and exposed 2205 samples - (a) HSI composite image of the control 2205 sample, highlighting evaluated 10x10-pixel areas from which the responses are averaged, (b) spectral responses from the control 2205 sample in the VNIR region, (c) spectral responses from the control 2205 sample in the SWIR region, (d) HSI composite image of the exposed 2205 sample, highlighting evaluated 10x10-pixel areas from which the responses are averaged, (e) spectral responses from the exposed 2205 sample in the VNIR region, and (f) spectral responses from the exposed 2205 sample in the SWIR region.

darker area of the sample surface. However, the VNIR responses extracted from the exposed 2205 sample (Fig. 5(e)), which would be expected to show corrosion in some degree, present a similar behavior to that found in the 316Ld case, where a curve appears in the range 400-700 nm. This would suggest that the spectral response of corrosion for both 316L and duplex 2205 in the VNIR region is similar.

A similar analysis was applied to these samples in the SWIR region of the spectrum. Fig. 5(c) shows three spectral responses from the control 2205 sample, while Fig. 5(f) does the same for the exposed 2205 sample. A visual inspection does not reveal conclusive differences in the SWIR responses, only a reduction in the overall reflectance intensity for some cases, which could be linked to the presence of corrosion [41]. In fact, a similar reduction in the overall reflectance intensity was already detected in the 316Ld case (see Fig. 4(c)).

C. *Characterizing Corrosion through Hyperspectral Imaging*

As seen in previous sections, the SWIR spectral responses for 316L steel in Fig. 4(c) are significantly different to the SWIR responses for 2205 steel in Fig. 5(c, f). This difference is not unexpected, as there may be potentially different corrosion products being present depending on the material and corrosion evolution.

Unlike SWIR, the VNIR spectral responses are more consistent among materials, probably as HSI in this range mainly captures color information, which seems more stable than the features appearing in the SWIR (peaks likely related to hydroxides presence). At the same time, there is an obvious difference between the responses depending on the spectral range being evaluated (VNIR or SWIR). This clearly emphasizes the point that the CI concept needs to be configured for the specific material under analysis and the spectral range being used.

Therefore, the findings in previous sections would suggest that, while no conclusive/consistent features can be initially identified for corrosion in the SWIR region (significant peaks have been identified, likely related to hydroxides presence, but they will require further analysis), spectral responses in the VNIR region seem to consistently indicate the presence of corrosion by showing a curve in the 400-700 nm range. This is in line with previous work [12], [34], [40], and relates to the presence of red-like colors, which show a peak around 700 nm.

Although the presence of useful features in the SWIR cannot be discarded, further analysis in this work focused on the VNIR region. In the next experiment, the 316L filter and the overpack can were evaluated. These two samples were selected because a visual inspection suggested the presence of different stages of corrosion across their surfaces and, hence, the spectral responses were expected to capture these differences.

Fig. 6 shows different responses in the 316L filter and the overpack samples, expected to represent different stages related to no-corrosion, early corrosion, and more advanced corrosion, in yellow, green, and blue/cyan color, respectively. These responses would suggest that corrosion can be measured by evaluating the slope of the response in the 500-600 nm range, relatively flat for no-corrosion, but increasing as corrosion becomes more evident. Hence, initial/subtle changes in this slope could be used for early corrosion detection.

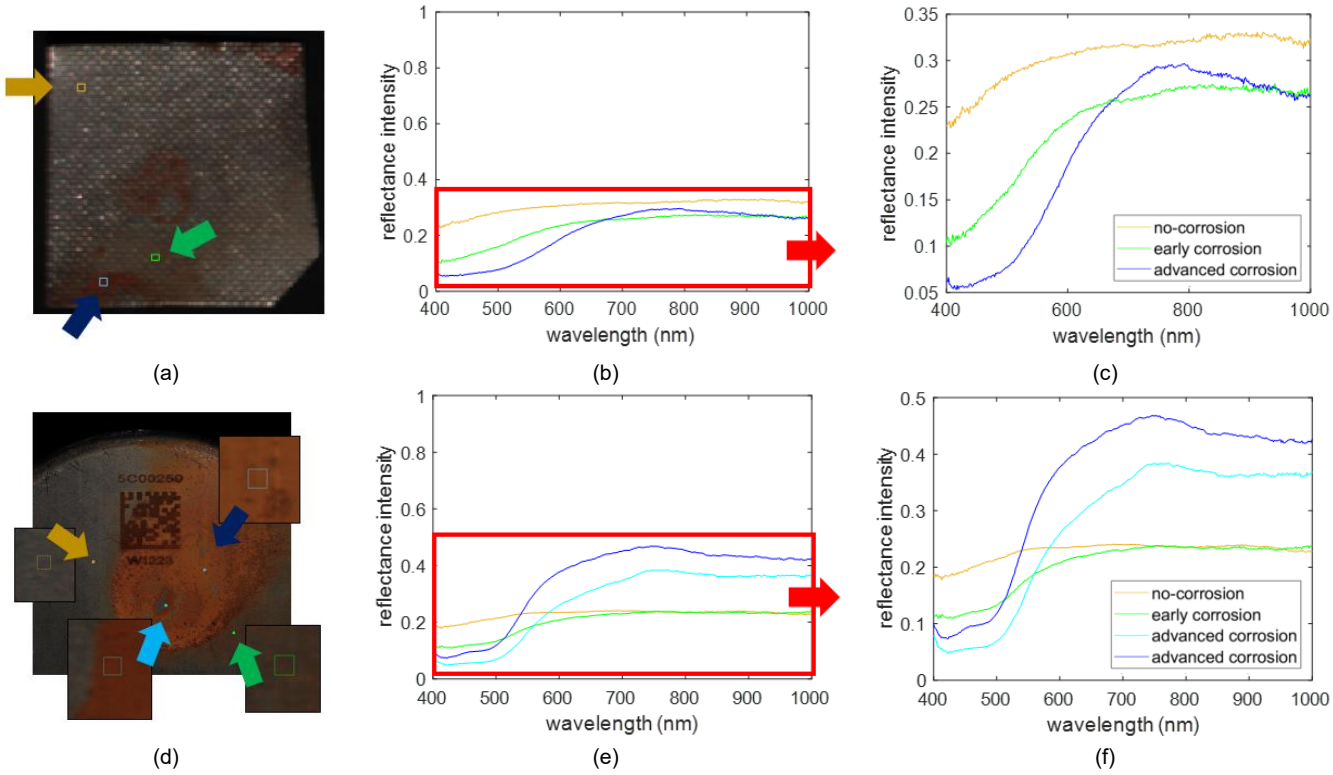

Fig. 6. Different corrosion stages identified in the 316L filter and the overpack samples - (a) HSI composite image of the 316L filter sample, highlighting evaluated 5x5-pixel areas from which the responses are averaged, (b) spectral responses in the VNIR region, and (c) zoomed-in spectral responses, (d) HSI composite image of the sample, highlighting evaluated 10x10-pixel areas from which the responses are averaged, (e) spectral responses in the VNIR region, and (f) zoomed-in spectral responses.

D. Mapping Corrosion through Hyperspectral Imaging

This new CI concept was applied to the two samples evaluated in the previous section, 316L filter and overpack can, where a CI value was generated for each pixel in the respective hyperspectral VNIR images. This led to a CI map for each case, maps that show the distribution of corrosion at different stages across the surface of the samples. The CI maps below include a colored bar for easy interpretation, where yellow, blue, and green colors correspond to no-corrosion, advanced corrosion, and intermediate cases, respectively.

The spectral reference (ref) used in ACD for the 316L filter and the overpack samples were the responses shown in blue color in Fig. 6(c) and Fig. 6(f), respectively, which are assumed to represent advanced corrosion in each case, and thus expected to lead to ACD values close to zero. Therefore, the b coefficients, which represent the ideal ACD values for advanced corrosion, were adjusted to $b = 0$. In order to adjust the a coefficient, the responses shown in yellow color in Fig. 6(c) and Fig. 6(f) were selected, which represent no-corrosion areas in each sample. The ACD values for these regions were 0.2058 and 0.2019, respectively, leading to rounded coefficients of $a = 0.2$ for both cases. The resulting CI maps are shown in Fig. 7.

Fig. 7(b) shows the CI map obtained for the 316L filter sample. This map presents the distribution of corrosion at different stages across the surface of the sample, showing advanced corrosion (dark blue color, with CI values close to one) in the bottom left corner, with a less advanced corrosion (lighter blue/green) in the middle part and the top right corner. Therefore, highly corroded areas are clearly highlighted, and the CI map also shows some dark yellow and green areas that could be interpreted as early corrosion or potential pre-corrosion. This would need confirmation from a subsequent chemical analysis.

The CI map for the overpack sample is available in Fig. 7(d). The different corrosion stages identified via the spectral responses in Fig. 6(f) were captured into different parts of the CI scale, with yellow, green, blue, and dark blue parts of the

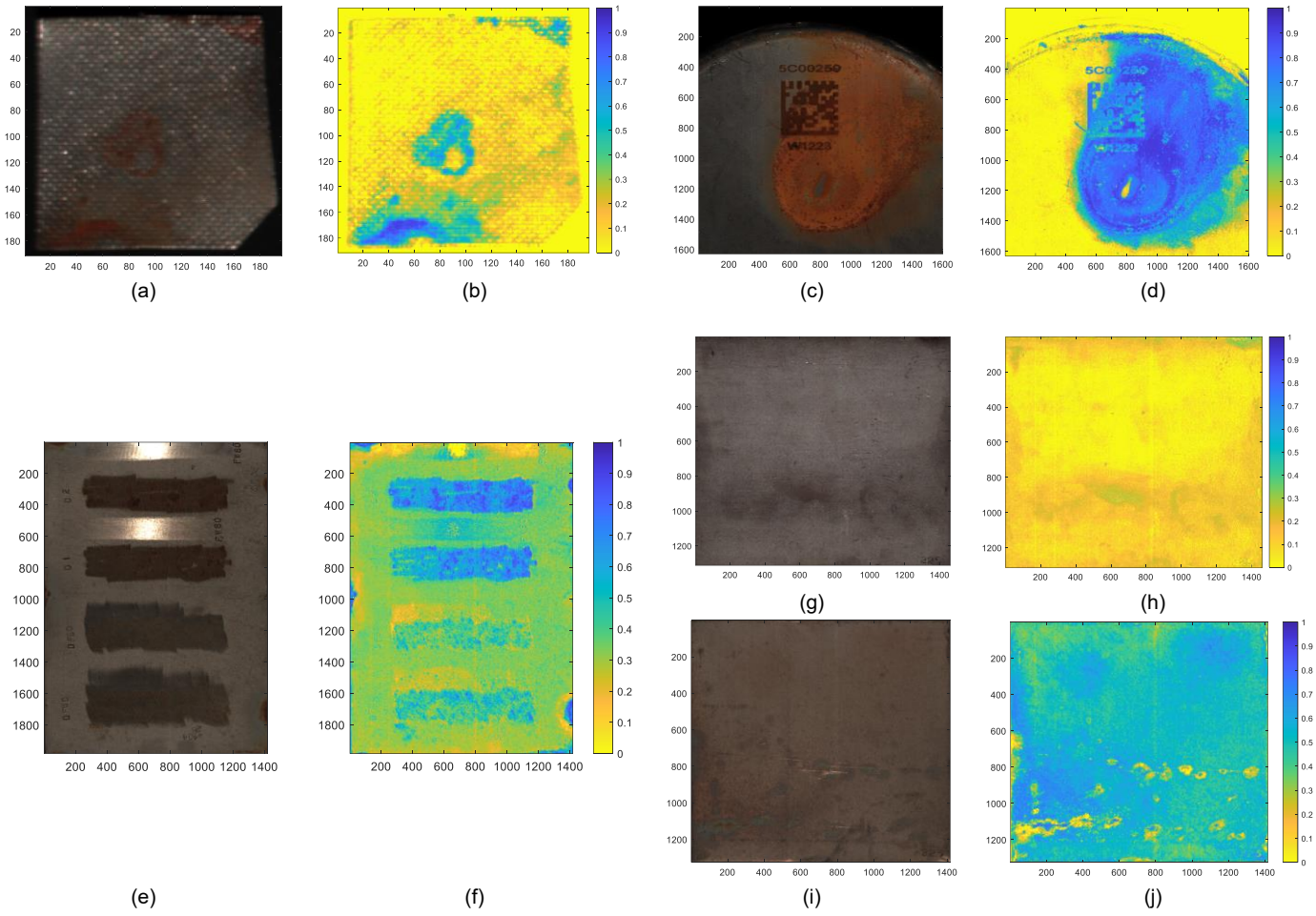

Fig. 7. CI maps for the samples based on the VNIR region.

Top left: CI map for the 316L filter sample - (a) HSI composite image of the sample, and (b) CI map based on the ACD score (with coefficients *a*=0.2, *b*=0).

Top right: CI map for the overpack sample - (c) HSI composite image of the sample, and (d) CI map based on the ACD score (with coefficients *a*=0.2, *b*=0).

Bottom left: CI map for the 316Ld sample - (e) HSI composite image of the sample, and (f) CI map based on the ACD score (with coefficients *a*=0.2, *b*=0).

Bottom right: CI map for the 2205 samples - (g) HSI composite image of the control 2205 sample, (h) CI map based on the ACD score (with coefficients *a*=0.11, *b*=0), (i) HSI composite image of the exposed 2205 sample, and (j) CI map based on the ACD score (with coefficients *a*=0.11, *b*=0).

color scale representing the four areas highlighted in Fig. 6(d). Again, the resulting map seems to show promise in translating the spectral responses from hyperspectral data into measurable corrosion intensity.

The CI map was also obtained for the other three samples evaluated in this work. For the 316Ld sample, the calibration of the a and b coefficients was similar to the one used for the previous samples, yielding the same values $b = 0, a = 0.2$. Also, the spectral reference (ref) used in ACD was the spectral response in blue color in Fig. 4(b), as this would be the response for advanced corrosion for this sample based on visual inspection.

The spectral reference (ref) for the control and exposed 2205 samples was the response in blue color in Fig. 5(e) for both cases (there was no advanced corrosion detected in the control 2205 sample). At the same time, the coefficient a was given the value of the ACD score between the spectral response used as reference (ref), from the exposed sample, and the spectral response in yellow color in Fig. 5(b), used as no-corrosion response, from the control sample. This led to the coefficients $b = 0, a = 0.11$ for both samples. Their resulting CI maps can be seen in Fig. 7(f), 7(h), and 7(j), respectively.

Fig. 7(f) shows the CI map for the 316Ld sample. According to the implemented CI, there is significant presence of corrosion in the four areas which were distressed prior to the exposure of the sample. The intensity of the corrosion seems to be higher in the two areas in the top part. There are some other regions highlighted as advanced corrosion, such as the top left and the bottom right corners. At the same time, there are some areas with close-to-zero values, especially in the top of the sample which, in some cases, could be related to specular reflections from the metal. The background of the sample, with more irregular values around the dark yellow and light green part of the scale, would suggest the presence of pre-corrosion or early corrosion. However, chemical analysis is required to confirm this.

Finally, Fig. 7(h) and Fig. 7(j) show the CI map for the control and exposed 2205 samples, respectively. This was the only case in which the CI was computed and calibrated using information from two independent samples of the same material, the first one stored and the second one exposed at Sellafield. Therefore, the behavior on these samples is of high interest to evaluate the CI performance. The resulting maps show that most pixels in the control sample exhibit a CI in the yellow part of the scale (close-to-zero values, i.e., no-corrosion), while most pixels in the exposed sample lead to a CI in the blue part of the scale, suggesting significant corrosion. This finding would be in line with expectations, as it was expected to find a relatively clean control sample, but significant corrosion in its exposed counterpart.

V. Conclusions

Intermediate level waste and special nuclear material are stored at the Sellafield nuclear site (Cumbria, UK) in stainless steel containers. Being stored above ground at Sellafield for decades, these packages are potentially subject to corrosion, especially atmospheric pitting corrosion. In recent years, several image processing techniques have been proposed for non-destructive detection of corrosion in metals, which could be used for long-term monitoring of these nuclear packages. However, HSI technology, with a much larger spectral resolution than conventional imaging, has been barely investigated for this purpose.

In this work, HSI was used to capture images of real samples from Sellafield and report the spectral responses of corrosion for different cases in two different spectral regions (VNIR 400-1000 nm, and SWIR 900-2500 nm). Based on the evolution of the spectral responses across different stages of corrosion, a new concept denoted as Corrosion Index (CI) was presented, in which every pixel in the hyperspectral image is given a value between zero and one, from no-corrosion to advanced corrosion, respectively. The CI requires calibration achievable via prior knowledge, using spectral responses of corrosion and no-corrosion for a given material as reference. After that, the CI can be applied to new samples of the same material. Also, while this concept was implemented through the ACD score, other underlying algorithms, e.g., curve fitting or other distance metrics, could be used for this.

Results show consistency in the CI maps generated for different cases, including 316L and control/exposed 2205 samples from the Sellafield atmospheric testing corrosion site, an overpack can with its base partially corroded due to PVC degradation, and a 316L filter on which corrosion was induced in the lab. The very next steps of this work aim at including comprehensive chemical characterization of the different corrosion products in the CI modeling by linking it to the hyperspectral responses. This will explore the physical, chemical and biological factors behind the respective spectral changes through standard measurements of different markers, combining multidisciplinary expertise covering hyperspectral analysis, image processing and chemistry analysis. Further exploration will also include the implementation of the CI through machine learning and deep learning methods, which will require comprehensive data for training.

VI. References

[1] A. R. Kazanjian, P. M. Arnold, W. C. Simmons, and E. L. D'Amico, "Gas generation results and venting study for transuranic waste drums," Rocky Flats Environmental Technology Site, Golden, Colorado, September 23, 1985.

[2] J. Zabalza et al, "Hyperspectral imaging based detection of PVC during Sellafield repackaging procedures," *IEEE Sensors Journal*, 2022.

[3] Y. Shao et al, "Automatic detection and imaging of rivet hole defects for aircraft structures with optimised sensor array using Eddy current method and image analysis," *IEEE Sensors Journal*, 2022.

[4] B. Yan et al, "Pulse-modulation Eddy current imaging for 3D profile reconstruction of subsurface corrosion in metallic structures of aviation," *IEEE Sensors Journal*, vol. 21, no. 24, pp. 28087-28096, 2021.

[5] E. Foster, G. Bolton, R. Bernard, M. McInnes, S. McKnight, E. Nicolson, C. Loukas, M. Vasilev, D. Lines, E. Mohseni, A. Gachagan, G. Pierce and C. Macleod, "Automated real-time Eddy current array inspection of nuclear assets," *Sensors*, vol. 22, 2022.

[6] Y. He et al, "Steel corrosion characterization using pulsed Eddy current systems," *IEEE Sensors Journal*, vol. 12, no. 6, pp. 2113-2120, 2012.

[7] Z. Abbasi et al, "Monitoring pH level using high-resolution microwave sensor for mitigation of stress corrosion cracking in steel pipelines," *IEEE Sensors Journal*, vol. 20, no. 13, pp. 7033-7043, 2022.

[8] K. Bouzaffour et al, "Development of an embedded UHF-RFID corrosion sensor for monitoring corrosion of steel in concrete," *IEEE Sensors Journal*, vol. 21, no. 10, pp. 12306-12312, 2021.

[9] H. Zhang et al, "Evaluation of atmospheric corrosion on coated steel using K -band sweep frequency microwave imaging," *IEEE Sensors Journal*, vol. 16, no. 9, pp. 3025-3033, 2016.

[10] J. Alonso-Valdesueir et al, "Highly sensitive undersea corrosion monitoring system," *IEEE Sensors Journal*, vol. 22, no. 12, pp. 12278-12287, 2022.
[11] A. Gunatilake et al, "Stereo vision combined with laser profiling for mapping of pipeline internal defects," *IEEE Sensors Journal*, vol. 21, no. 10, pp. 11926-11934, 2021.
[12] W. Rowley, Hyperspectral imaging for detection of corrosion on intermediate level nuclear waste containers, University of Birmingham, PhD Thesis, 2018.
[13] Headwall Photonics Inc., "VNIR 400-1000nm," [Online]. Available: https://www.headwallphotonics.com/products/vnir-400-1000nm [Accessed March 2022].
[14] Headwall Photonics Inc, "SWIR 900-2500nm," [Online]. Available: https://www.headwallphotonics.com/products/swir-900-2500nm [Accessed March 2022].
[15] P.-H. Chen, Y.-C. Yang and L. Chang, "Automated bridge coating defect recognition using adaptive ellipse approach," *Automation in Construction*, vol. 18, pp. 632-643, 2009.
[16] F. Bonnín-Pascual and A. Ortiz, "Corrosion detection for automated visual inspection," InTechOpen, 2014.
[17] H. Son, N. Hwang, C. Kim and C. Kim, "Rapid and automated determination of rusted surface areas of a steel bridge for robotic maintenance systems," *Automation in Construction*, vol. 42, pp. 13-24, 2014.
[18] L. Petricca, T. Moss, G. Figueroa and S. Broen, "Corrosion detection using A.I.: A comparison of standard computer vision techniques and deep learning model," in The Sixth International Conference on Computer Science, Engineering and Information Technology, 2016.
[19] F. Feliciano, F. Leta and F. Mainier, "Texture digital analysis for corrosion monitoring," *Corrosion Science*, vol. 93, pp. 138-147, 2015.
[20] S. Ahuja and M. Shukla, "A survey of computer vision based corrosion," in Information and Communication Technology for Intelligent Systems, 2017.
[21] T. Gibbons, G. Pierce, K. Worden and I. Antoniadou, "A Gaussian mixture model for automated corrosion detection in remanufacturing," in 16th International Conference on Manufacturing Research, 2018.
[22] V. Bondada, D. Pratihar and C. Kumar, "Detection and quantitative assessment of corrosion on pipelines through image analysis," *Procedia Computer Science*, vol. 133, pp. 804-811, 2018.
[23] I. Ivasenko and V. Chervatyuk, "Detection of rust defects of protective coatings based on HSV color model," in IEEE 2nd Ukraine Conference on Electrical and Computer Engineering (UKRCON), Lviv, Ukraine, 2019.
[24] D. Naik, H. Sajid, R. Kiran and G. Chen, "Detection of corrosion-indicating oxidation product colors in steel bridges under varying illuminations, shadows, and wetting conditions," *Metals*, vol. 1439, no. 10, 2020.
[25] Y. Zhao, G. Wang, H. Zhang and L. Li, "Material corrosion classification based on deep learning," *Chemical Engineering Transactions*, vol. 71, pp. 775-780, 2018.
[26] N.-D. Hoang and V.-D. Tran, "Image processing-based detection of pipe corrosion using texture analysis and metaheuristic-optimized machine learning approach," *Computational Intelligence and Neuroscience*, 2019.
[27] N.-D. Hoang, "Image processing-based pitting corrosion detection using metaheuristic optimized multilevel image thresholding and machine-learning approaches," *Mathematical Problems in Engineering*, 2020.
[28] M. Khayatazad, L. De Pue and W. De Waele, "Detection of corrosion on steel structures using automated image processing," *Developments in the Built Environment*, vol. 3, 2020.
[29] T. Papamarkou, H. Guy, B. Kroencke, J. Miller, P. Robinette, D. Schultz, J. Hinkle, L. Pullum, C. Schuman, J. Renshaw and S. Chatzidakis, "Automated detection of corrosion in used nuclear fuel dry storage canisters using residual neural networks," *Nuclear Engineering and Technology*, vol. 53, pp. 657-665, 2021.
[30] Y. Zhang, L. Deng, H. Zhu, W. Wang, Z. Ren, Q. Zhou, S. Lu, S. Sun, Z. Zhu, J.M. Gorriz, and S. Wang, "Deep learning in food category recognition," *Information Fusion*, no. 98, 2023.
[31] L. Deng, F. Cheng, X. Gao, W. Yu, J. Shi, L. Zhou, L. Zhang, M. Li, Z. Wang, Y-D. Zhang, and Y. Lv, "Hospital crowdedness evaluation and in-hospital resource allocation based on image recognition technology," *Scientific Reports*, vol. 13, no. 299, 2023.
[32] L. Deng, S.-H. Wang, and Y.-D. Zhang, "ELMGAN: A GAN-based efficient lightweight multi-scale-feature-fusion multi-task model," *Knowledge-Based Systems*, vol. 252, 2022.
[33] C.-I. Chang, Hyperspectral Imaging: Techniques for Spectral Detection and Classification, *Springer Science & Business Media*, 2003.
[34] E. Simova and P. Rochefort, "Active spectral imaging nondestructive evaluation (SINDE) camera," CNL Nuclear Review, 2016.
[35] E. Catelli, L. Randeberg, H. Strandberg, B. Alsberg, A. Maris and L. Vikki, "Can hyperspectral imaging be used to map corrosion products on outdoor bronze sculptures?," *J. Spectral Imaging*, vol. 7, 2018.
[36] M. Antony, C. Sandeep and M. Matham, "Monitoring system for corrosion in metal structures using a probe based hyperspectral imager," in Seventh International Conference on Optical and Photonic Engineering, Phuket, Thailand, 2019.
[37] M. Antony, C. Sandeep and M. Matham, "High resolution probe for corrosion monitoring using hyper spectral imaging," in AIP, 2021.
[38] R. Kobayashi, H. Katayama and T. Akashi, "Evaluation of corrosion resistance of steel materials by hyperspectral analysis of corrosion products," IOPscience, 2020.
[39] G. Chen, "Hyperspectral imaging analysis for mechanical and chemical properties of concrete and steel surfaces," Missouri University of Science and Technology, 2020.
[40] D. Lavadiya, H. Sajid, R. Yellavajjala and X. Sun, "Hyperspectral imaging for the elimination of visual ambiguity in corrosion detection and identification of corrosion sources," *Structural Health Monitoring*, vol. 0, no. 0, pp. 1-16, 2021.
[41] K. Yang, C. Shi, Y. Guo, X. Zhang, C. Li and G. Wu, "Non-contact identification method for carbon steel corrosion grade of transmission tower based on hyperspectral technology," in International Conference on Electrical Materials and Power Equipment (ICEMPE), 2021.
[42] T. De Kerf, G. Pipintakos, Z. Zahiri, S. Vanlanduit and P. Scheunders, "Identification of corrosion minerals using shortwave infrared hyperspectral imaging," *Sensors*, vol. 22, no. 407, 2022.
[43] Headwall Photonics Inc, "Hyperspectral Sensors," [Online]. Available: https://www.headwallphotonics.com/products/hyperspectral-sensors [Accessed March 2022].
[44] G, G. ElMasry and D. W. Sun, "Principles of hyperspectral imaging technology," in Hyperspectral Imaging for Food Quality Analysis and Control, London, Elsevier, 2010, pp. 32-36.
[45] J. Zabalza, J. Ren and S. Marshall, "'On the fly' dimensionality reduction for hyperspectral image acquisition," in 23rd European Signal Processing Conference (EUSIPCO), 2015.
[46] National Institute of Standards and Technology, "Cosine distance, cosine similarity, angular cosine distance, angular cosine similarity," 2018. [Online]. Available: www.itl.nist.gov [Accessed 2022].
[47] S. Cai, G. K. Georgakilas, J. L. Johnson and G. Vahedi, "A cosine similarity-based method to infer variability of chromatin accessibility at the single-cell level," *Frontiers in Genetics*, vol. 9, 2018.

Jaime Zabalza (Member, IEEE) received the M.Eng. degree in industrial engineering from the Universitat Jaume I (UJI), Castellón, Spain; and the M.Sc. and Ph.D. degrees in Electronic and Electrical Engineering from the University of Strathclyde, Glasgow, U.K. He was awarded the IET Image & Vision Section prize for best Ph.D. thesis for his work in hyperspectral remote sensing.

He is currently a Chancellor's Fellow (Lecturer), within the Advanced Nuclear Research Centre (ANRC) at the Department of Electronic and Electrical Engineering, University of Strathclyde. His research interests include hyperspectral data analysis as well as signal and image processing in a wide range of applications.

Paul Murray received the M.Eng. and Ph.D. degrees in Electronic and Electrical Engineering from the University of Strathclyde, Glasgow, U.K., in 2008 and 2012, respectively.

He is a Reader at the University of Strathclyde in the department of Electronic and Electrical Engineering. His research interests include image processing, hyperspectral imaging & analysis, feature extraction, machine learning and artificial intelligence.

Stuart Bennett joined the University of Strathclyde in 2018, to research algorithms for compressive hyperspectral imaging to be used on a novel satellite-based imager. Since then, he has undertaken a number of projects with partners in the UK nuclear industry, developing automated vision-based monitoring and inspection tools.

His previous industrially oriented work, while in Cambridge University's Signal Processing group, included collaborations with a medical devices start-up, Google, British Cycling and an America's Cup racing team.

These projects spanned many research topics in computer vision and image processing, focusing on analysis and measurement outputs, such as non-invasive recognition of lung function disease states, on-vehicle tyre defect detection, and the production of aerodynamic metrics. A consistent theme throughout has been the necessity to deliver fast, accurate and robust automation, working in the most challenging conditions.

Andrew Campbell received the EngD degree in 2018 for his work on image segmentation and the application of these technique to automate the analysis of metal microstructures in the manufacturing sector. Since then he has worked as a post-doctoral researcher within the signal and image processing group

His main research interests are in the area of signal and image processing and hyperspectral data analysis using state-of-the-art Machine Learning algorithms and more traditional techniques. His research portfolio is highly collaborative and interdisciplinary with most projects targeting the development of techniques towards industrial applications.

His hyperspectral imaging work includes nuclear inspection, space object analysis and classification and detection of hazardous substances in soils and in the food industry, among others.

Prof Stephen Marshall received a 1st class honors degree in Electrical and Electronic Engineering from the University of Nottingham and a PhD in Image Processing from University of Strathclyde. In between he worked at Plessey Office Systems, Nottingham, University of Paisley and the University of Rhode Island, USA.

He established the Hyperspectral Imaging Centre at the University of Strathclyde which provides solutions to industrial problems through applied research and Knowledge Exchange.

He has published over 200 conference and journal papers on these topics including IET, IEEE, SPIE, SIAM, ICASSP, VIE and EUSIPCO. He has also been a reviewer for these and other journals and conferences.

He is a Fellow of the Institution of Engineering and Technology and Senior member of the IEEE. He has also been successful in obtaining research funding from National, International and Industrial sources. These sources include EPSRC, EU, Rolls Royce, BT, DERA, the BBSRC, Scottish Enterprise and Innovate UK.

Stephen is a Professor in the Department of Electronic and Electrical Engineering and Director of the Institute for Sensors, Signals and Communications.

He is also the lead academic for the Vertically Integrated Project for Sustainable Development Program at Strathclyde.

Jinchang Ren (Senior Member, IEEE) received his B. Eng. degree in computer software, M.Eng. in image processing, and D. Eng. in computer vision, all from Northwestern Polytechnical University, Xi'an, China. He was also awarded a Ph.D. degree in Electronic Imaging and Media Communication from the University of Bradford, Bradford, U.K.

Currently he is a full Professor of Computing Sciences, Transparent Ocean Lead, and Director of the Hyperspectral Imaging Lab at the National Subsea Centre (NSC), also Director of NSC International PGR Academy, Robert Gordon University, Aberdeen, U.K.

Jinchang is a Senior Member of IEEE, and Lifetime Achievement Fellow of Marquis Who's Who. His research interests focus mainly on hyperspectral imaging, image processing, computer vision, big data analytics and machine learning, with a research portfolio over £6 million. He has published 300+ peer reviewed journal/conferences articles, and acts as an Associate Editor for several international journals including IEEE TGRS and J. of the Franklin Institute et al. He has also chaired and co-chaired a number of conferences and workshops. His students have received many awards, such as the Best PhD thesis from IET Image and Vision Section (for Jaime Zabalza's work in hyperspectral image analysis) in 2016 and various conferences/workshops.

Yijun Yan (M'18) received the M.Sc. and Ph.D. degrees in electrical and electronic engineering from the University of Strathclyde, Glasgow, U.K. in 2013 and 2018, respectively. He is currently a Research Fellow with Robert Gordon University, Aberdeen, U.K. His research interests include HSI, pattern recognition, computer vision, and machine learning.

Robert Bernard is a Senior Technology Manager at Sellafield Ltd. He leads at team of scientists and engineers specialised in the safe storage and management of Special Nuclear Materials on the Sellafield site.

To achieve this, Robert works closely with his team to engage with the academic community and industrial partners in the Sellafield supply chain to ensure that he and his team have the best technology and expertise (internally and within the supply chain) to ensure he can continue to effectively inspect, monitor, and keep-safe the SNM products for which he and his team are responsible.

Steve Hepworth (University Lead, Sellafield Ltd, UK) gained a BSc (hons) in Applied Physics (UCLAN) 1995, an MSc in Medical Physics (Aberdeen) 1996 and a PhD in Medical Radiation Physics (Surrey) in 2000.

He has over 20 years of experience in the civil nuclear industry, initially specializing in radiation measurement techniques on legacy infrastructure and operational reprocessing plants. His last 15 years at Sellafield Ltd have been spent in Nuclear Decommissioning R&D during which time he has designed and commissioned studies on a variety of decommissioning projects including remote cutting methods, novel radiometric monitoring, unmanned aerial vehicles, hydrogen detection, energy harvesting, decontamination and virtual environments. During this time, he also led a multi-disciplinary team examining methods of detecting and mitigating leaks from the Magnox Swarf Storage Silo.

Steve is now a part of the senior leadership team in science and technology at Sellafield Ltd with the responsibility of developing University relationships and collaborations. He is a Chartered Physicist and Fellow of the Institute of Physics.

Simon Malone (Research Lead for Measurement and Analysis, Sellafield Ltd.) gained a BSc. in Applied Chemistry, (UWE Bristol 1996), an MSc. in Analytical Chemistry (UEA Norwich, 1997) and a PhD in Raman Spectroscopy (UEA Norwich 2001).

Simon has a background in spectroscopy and polymers and he is a chartered chemist who researches new tools and techniques to help Sellafield Ltd. achieve its mission sooner.

Neil Cockbain studied at the University of Central Lancashire and in 1987, joined the Research and Development Department at the Sellafield site. Within the National Nuclear Laboratory (NNL), Neil has experience on a variety of radiometric, physical and optical instrument projects, including experimental rigs, laboratory programmes, design, manufacture and deployment of bespoke instruments for in-situ analysis.

Neil has worked on software modifications to maintain instruments in the THORP process for Sellafield Ltd (SL) and has since contributed on instrumentation projects for several nuclear sites and industrial processes. Neil has a foundation knowledge of instrumentation and software design, which to date has focussed primarily on deployment of bespoke instruments, such as hyperspectral image processing and analysis, in the nuclear environment.

He now leads a team of research technologists, being a Capability Manager, and brings together new technologies researched by universities and the nuclear industry to realise low TRL to become a working instrument for decommissioning, condition monitoring and inspection. His research interests include wireless communication, imaging equipment and radiation sensing technology in a wide range of applications.

Douglas Offin studied at University of Southampton, where he completed his PhD in Acoustoelectrochemical Characterisation of Cavitation and achieved a MChem: Chemistry, 1st Class (Hons). Doug has worked for NNL in the Instrumentation and In-Stu Analysis (IIA) team since October 2014 and in this role, he has gained experience of sensor and instrument development for applications in the nuclear environments.

He also has a wide-ranging experience in research projects for several customers including design of experiments, data analysis and result dissemination via reports, journal articles and presentations. At NNL, Doug has sought new challenges and led projects from bid preparation through to delivery to the customer in areas such as Package Performance, Future Decommissioning, Instrument development, deployment and support, and Innovation/R&D/University Interactions. His research interests include sensor deployment, image processing and analysis in a wide range of applications.

Craig Holliday studied at the University of Bath, where he completed a BSc (Hons) in Biology. He joined NNL in 2020, following previous experience as an Analytical Specialist in the polymer industry where he focussed on microscopic (SEM, AFM) and spectroscopic (FTIR) characterisation of materials, becoming a fellow of the Royal Microscopical Society.

His initial work in the nuclear industry was with the In-Situ Analysis (IIA) team, developing an understanding of analytical and instrumentation requirements across a range of challenging environments. Building on this and his analytical background, his current work now focuses on microscopy in the nuclear environment for Post Irradation Examination (PIE).